https://dx.doi.org/https://doi.org/10.1016/j.intermet.2021.107399

Alloying effects on phase stability, mechanical properties, and deformation behavior of CoCrNi-based medium-entropy alloys at low temperatures

S. Qiu[a], G.P. Zheng[a], Z.B. Jiao[a,b,*]

[a] *Department of Mechanical Engineering, The Hong Kong Polytechnic University, Hong Kong, China*

[b] *The Hong Kong Polytechnic University Shenzhen Research Institute, Shenzhen 518057, China*

** Corresponding authors: zb.jiao@polyu.edu.hk*

Abstract

Alloying plays an important role in determining the phase stability and mechanical behavior of medium/high-entropy alloys (M/HEAs). In this work, the effects of Al, Ti, Mo, and W additions on the phase stability, strengthening behavior, and stacking fault energies of CoCrNi alloys are quantitatively investigated by using first-principles calculations. Our results reveal that the Al, Ti, and W additions enhance the structural stability of metastable face-centered cubic structures, whereas Mo is in favor of the formation of hexagonal close-packed structures at low temperatures. Through analyzing the elastic moduli and lattice mismatch based on a Labusch-type model, we show that the solute strengthening effect decreases in the order W > Mo > Ti > Al. The compositional dependence of intrinsic stacking fault energy (ISFE) and unstable stacking fault energy (USFE) of CoCrNi MEAs was calculated, and the results indicate that the Al, Ti, Mo and W additions significantly reduce the USFE, leading to a reduction in the energy barriers of dislocation slips. The alloying effects on the deformation behaviors of CoCrNi MEAs are discussed in terms of the ratio of ISFE to the energy barrier of dislocation slips. The present study

not only sheds light on the fundamental understanding of phase stability and deformation mechanisms of M/HEAs but also provides useful guidelines for the alloy design of advanced M/HEAs with superior mechanical properties.

Keywords: medium-entropy alloy, alloying effect, phase stability, mechanical property, deformation behavior, first-principles calculation.

1. Introduction

Medium/high-entropy alloys (M/HEAs) are loosely defined as simple solid-solution alloys consisting of three or more principal elements, the concept of which evokes the vastness of composition space to design novel alloys [1-4]. A family of face-centered cubic (fcc) HEAs containing 3d transition metal elements, such as Co, Cr, Fe, Ni, and Mn, has attracted considerable interest due to their unusually superior mechanical properties at low temperatures [5]. For instance, the CoCrFeNiMn HEA exceeds the toughness of most pure metals and most metallic alloys and has a strength comparable to that of structural ceramics [6,7]. Additionally, the CrCoNi ternary MEA displays even better properties, approaching the best damage tolerance on record [8]. Experimental and theoretical studies have demonstrated that the superior mechanical properties of the M/HEAs are related to the unique deformation mode involving the formation of intrinsic stacking faults and deformation twins at low temperatures [9]. However, the yield strength of the equiatomic fcc M/HEAs are relatively low, limiting their applications in structural engineering. To achieve more desirable yield strength for engineering applications, strengthening of M/HEAs is necessary.

Alloying has been considered as an effective method to improve the mechanical properties of M/HEAs [10-14]. Particularly, solute strengthening is of technological importance for fcc M/HEAs. Solute additions can influence the elastic interaction between the local stress fields and surrounding dislocations. Based on the model of elasticity, the elastic interaction can be simply described by the lattice distortion and elastic modulus mismatch [15], which impedes the glide of dislocations, resulting in a solute strengthening effect. A reduced model based on the Labusch's approach was proposed by Varvenne *et al*. [16] to quantify solute strengthening of M/HEAs, which agrees well with the experimental data for the CoCrNi-based alloys [17,18]. The results showed that the solute strengthening effects in CoCrNi, CoCrFeNi and CoCrFeNiMn are several hundred MPa at 0 K [19].

In addition, alloying also plays an important role in the deformation behaviors of fcc M/HEAs [20]. The formation of high densities of stacking faults and deformation twins is considered as an important mechanism to overcome the strength-ductility trade-off in the M/HEAs [11], which can be controlled by tuning the stacking fault energy (SFE) [21]. In an fcc structure, the intrinsic stacking faults (ISFs) can be created by the glide of a Shockley partial dislocation during deformation, whereas the *n*-layer deformation twins can be obtained by shearing *n* successive (111)-layers [22]. A high positive ISF energy (ISFE) leads to the easy motion of full-slip and multiplication of the dislocations. A low ISFE tends to induce deformation twinning, whereas a negative ISFE suggests that the ISFs are easy to form. For example, a high density of ISFs was experimentally observed in a CoCrNi alloy at low temperatures [23], which is consistent with the

negative ISFE by using the first-principles calculations [24]. The SFE is known to be very sensitive to alloying additions. For example, Laplanche *et al.* [25] reported that the ISFE of the CoCrNi alloy increases with the addition of Fe, making the twinning stress to be reached at high plastic strains; they also suggested that the later appeared nano-twinning in the CoCrFeNi alloy than in the CoCrNi alloy is responsible for the reduced ultimate strength, ductility, and toughness at 77 K.

From the strengthening point of view, large atoms, such as Al, Ti, Mo, and W, would induce large lattice distortions and hence are expected to provide effective strengthening effects in 3d transition metal M/HEAs. In fact, in recent experimental studies large atoms have been shown to significantly affect the mechanical properties of fcc M/HEAs, confirming their effectiveness in improving the mechanical properties [26-29]. However, the fundamental mechanisms of the alloying effects on the phase stability, strengthening, and deformation behavior are still elusive.

In this work, the effects of large atoms, including Al, Ti, Mo, and W, on the phase stability, elastic properties, solute strengthening, SFE, and deformation behavior of CoCrNi-based MEAs were systematically investigated by using first-principles calculations based on the density functional theory. Specifically, the total energy of the fcc and hexagonal close-packed (hcp) phases, lattice distortion, elastic properties, solute strengthening, and SFE of the $CoCrNiM_x$ (M = Al, Ti, Mo, and W; x = 0 – 0.1) alloys were systematically calculated. The emphasis was placed on the fundamental understanding of the alloying effects on the phase stability, strengthening, and deformation mechanisms of fcc MEAs.

2. Methods

Based on the density functional theory, the exact muffin-tin orbitals (EMTO) method in combination with the coherent potential approximation (CPA) was used for the self-consistent and total energy calculations [30], which has been widely used for the investigations of structural stability, mechanical properties, and SFE of M/HEAs [31,32]. The EMTO-CPA method uses a mean-field type of averaging, which enables the description of M/HEAs in terms of an effective medium matrix constructed in a way that it represents, on the average, the physical properties of the alloys. The paramagnetic state was simulated by the disordered local moment (DLM) model [33]. The exchange-correlation functional was carried out within the generalized gradient approximation in the form of Perdew, Burke, and Ernzerhof (PBE) [34]. The Green's function was calculated by using 16 complex energy points on a semicircular contour including the valence states. The basis set included the *s*, *p*, *d*, and *f* states. The *k*-points ranging from 3125 to 24389 were used to sample the irreducible wedge of Brillouin zone to ensure the accuracy of calculated total energies within 10^{-2} mRy/atom.

The equilibrium volume and polycrystalline bulk modulus (B) were derived from an exponential Morse-type function. By fitting the energies against the orthorhombic strain tensors, the tetragonal shear modulus [$(C_{11} - C_{12})/2$] can be obtained. The C_{11} and C_{12} were then obtained with the tetragonal shear modulus [$(C_{11} - C_{12})/2$] and bulk modulus [$(C_{11} + 2C_{12})/3$]. The elastic constant of C_{44} were evaluated by fitting the energies against the monoclinic strain tensors. The

polycrystalline elastic properties of shear modulus (G), Poisson's ratio (v), and Young's modulus (E) can be given by

$$G = \frac{G_R + G_V}{2}, \tag{1}$$

$$G_{\mathrm{R}} = \frac{5C_{44}(C_{11} - C_{12})}{4C_{44} + 3(C_{11} - C_{12})}, \tag{2}$$

$$G_{\mathrm{V}} = \frac{G_{11} - G_{12} + 3G_{44}}{5}, \tag{3}$$

$$v = \frac{3B - 2G}{2(3B + G)}, \tag{4}$$

$$E = \frac{9BG}{3B + G}, \tag{5}$$

where G_R and G_V are the Reuss and Voigt averages of the shear modulus, respectively.

The generalized SFE profiles for the $<11\bar{2}>(111)$ slip system of fcc systems were calculated by adopting a six-layer supercell. The schematic of planar fault path on (111) planes for the ideal fcc structure, unstable stacking fault (USF), and ISF is shown in Fig. 1. For the details about the formation of USF and ISF, we refer to Ref. [35]. The USF energy (USFE), γ_{usf}, and ISFE, γ_{isf}, can be described by

$$\gamma_{usf} = \frac{E^{usf} - E^{fcc}}{A}, \tag{6}$$

$$\gamma_{isf} = \frac{E^{isf} - E^{fcc}}{A}, \tag{7}$$

where A is the area of the basal plane of supercell, E^{fcc} is the total energy of the ideal fcc structure (See Fig. 1a), and E^{usf} and E^{isf} are the total energies of USF (Fig. 1b) and ISF (Fig. 1c), respectively.

3. Results and discussion

3.1 Lattice parameters and phase stability

The lattice parameters of the CoCrNi-based alloys are shown in Fig. 2 as a function of the Al, Ti, Mo, and W contents. The Wigner-Seitz (W-S) radius of CoCrNi is 2.604 Bohr, which is in good agreement with the theoretical results (2.604 Bohr) at 0 K [36] and experimental data (2.606 Bohr) at 77 K [37], demonstrating a high reliability and accuracy of our calculated lattice parameters. With the addition of Al, Ti, Mo, and W to the CoCrNi alloy, the W-S radius increases significantly, reaching 2.626, 2.642, 2.657, and 2.668 Bohr for the alloys with 10 at.% Al, Ti, Mo, and W, respectively. The larger lattice parameters of the CoCrNi-based alloys with the W and Mo additions than those with the Ti and Al additions suggest that W and Mo changes the lattice parameters more efficiently.

To characterize the effect of alloying additions on the phase stability, we studied the energy difference among the hcp, fcc and bcc phases. The energy difference (ΔE) at 0 K is described by

$$\Delta E_{hcp-fcc} = E_{hcp} - E_{fcc}, \tag{8}$$

$$\Delta E_{bcc-fcc} = E_{bcc} - E_{fcc}, \tag{9}$$

where E_{hcp}, E_{fcc}, and E_{bcc} are the total energies of the hcp, fcc, and bcc phases, respectively. For comparison purpose, the energy difference of CoCrNi was used as a reference value. The energy difference between the hcp and fcc phases (E_{hcp}- E_{fcc}) and between the bcc and fcc phases (E_{bcc}-

E_{fcc}) of the CoCrNi-based alloys are shown in Fig. 3a and b, respectively, as a function of the Al, Ti, Mo and W additions. The calculation results reveal that the energy difference between the bcc and fcc phases is large positive (>0.02 eV), indicating that the bcc phase is far more unstable than the fcc phase in the studied alloys. In contrast, the energy difference between the hcp and fcc phases is slightly negative (<0.01 eV), indicating that the hcp phase is slightly more stable than the fcc phase. In the following, we focus on the compositional dependence of stability between the fcc and hcp phases. The ΔE of CoCrNi is -0.0071 eV, indicating that the hcp phase is more stable than the fcc phase at 0 K. Considering that the fcc phase, rather than the hcp phase, was experimentally observed in the CoCrNi alloy at low temperatures [8], it generally considered that the fcc phase is in a metastable state [38]. Similar phenomenon has also been reported in the CoCrFeNiMn alloy [39].

With the Al additions, the ΔE increases from -0.0071 eV/atom for the CoCrNi alloy to -0.0054 eV/atom for the alloy with 4 at.% Al, to -0.0045 eV/atom for the alloy with 7 at.% Al, and to -0.0039 eV/atom for the alloy with 10 at.% Al. These results indicate that Al acts as an fcc stabilizer in the CoCrNi-based alloys at 0 K. In addition, adding Ti to the CoCrNi alloy also results in an increase in the ΔE, suggesting that Ti also enhances the stability of the fcc phase. Adding W to the CoCrNi alloy also increases the ΔE, but at a slow rate. On the contrary, alloying Mo results in a decrease in the ΔE from -0.0071 eV/atom for the CoCrNi alloy to -0.0081 eV/atom for the alloy with 4 at.% Mo and to -0.0089 eV/atom for the alloy with 10 at.% Mo, indicating that Mo acts as an hcp stabilizer in the CoCrNi-based alloy at 0 K. These observations suggest that control of the

type and concentration of alloying elements is an effective technique to tailor the phase stability of M/HEAs.

3.2 *Elastic properties and solute strengthening*

Generally, the lattice distortion and elastic modulus misfit contribute to the solute strengthening of crystalline alloys. The lattice distortion can be determined by comparing a distorted lattice and its ideal counterpart lattice containing atoms with an equivalent average atomic volume, and the schematic model is displayed in Fig. 4. This model is based on the approximation that each element can be seen as a “solute” embedded in the average effective medium matrix of the surrounding environment. Based on this approximation, the equivalent average atomic volume can be calculated, and then the difference between the atomic volume of each solute and the equivalent average atomic volume can be determined. The lattice distortion can thus be calculated by the sum of weighted squares of all the volume differences. This model has an advantage over the existing models based on average atomic radius, because this model does not require the reliability of Vegard's law by using empirical atomic radii of elements, nor rely on the validity of an assumption that different elements crystallize into the same structure. The effects of alloying additions on the lattice distortion (δ) can be expressed as

$$\delta=\sum_{n=1}^{N} C_n \Delta V_n^{\,2}\,, \tag{10}$$

where C_n is the concentration of element n in the N-element alloy, and ΔV_n describes the volume difference between the alloys with and without alloying additions, which is given by

$$\Delta V_n^2 = (\overline{V_N} - V_n)^2, \quad (11)$$

where $\overline{V_N}$ is the averaged volume per atom of the alloy, as summarized in Table 1, and V_n is the effective volume of element n in the N-element alloy. The volumes, including V_1, $V_2 \ldots V_N$, satisfy

$$\overline{V_N} = x_1 V_1 + x_2 V_2 + \ldots + x_N V_N, \quad (12)$$

$$1 = x_1 + x_2 + \ldots + x_n, \quad (13)$$

where x_1, $x_2 \ldots x_N$ are the concentrations of elements in the N-element alloy. With input the volume values as listed in Table 1, the effective volumes of Co, Cr, Ni, Al, Ti, Mo, and W in the CoCrNi-based alloys were obtained and are summarized in Table 2. The calculated effective volumes of Co, Cr, Ni, and Al are 69.0, 80.1, 73.0 and 92.8 $Bohr^3$/atom, respectively, which are in good agreement with the experimental results (75.0 $Bohr^3$/atom for Co, 82.8 $Bohr^3$/atom for Cr, 73.8 $Bohr^3$/atom for Ni, and 94.5 $Bohr^3$/atom for Al) [40, 41].

The predicted lattice distortions (δ) of the $CoCrNiM_x$ alloys are shown in Table 1. It is evident that CoCrNi has the smallest lattice distortion (δ = 21.1) among all the studied alloys. With the alloying addition of Al, Ti, Mo, and W, the lattice distortion increases substantially. The lattice distortion of the CoCrNi-based alloys is in the order $\delta((CoCrNi)_{0.9}W_{0.1}) > \delta((CoCrNi)_{0.9}Mo_{0.1}) > \delta((CoCrNi)_{0.9}Ti_{0.1}) > \delta((CoCrNi)_{0.9}Al_{0.1}) > \delta(CoCrNi)$. It is noted that the effective volume of W (129.8 $Bohr^3$/atom) is larger than that of Mo (120.7 $Bohr^3$/atom), Ti (106.7 $Bohr^3$/atom), and Al

(92.8 $Bohr^3$/atom), as shown in Table 2. Therefore, it is reasonable to believe that the alloying element with a large effective volume induces a large lattice distortion.

To investigate the effects of alloying additions on the elastic properties, the elastic constants of the CoCrNi-based alloys with different alloying additions were calculated, and the results are summarized in Table 3. It is evident that the values of C_{11}, C_{12} and C_{44} of the CoCrNi-based alloys decrease with the Al, Ti, Mo, and W additions. The C_{11} varies from 296 GPa (CoCrNi) to 248 GPa ($(CoCrNi)_{0.9}Ti_{0.1}$). The decrease of C_{11} for $(CoCrNi)_{0.9}Al_{0.1}$, $(CoCrNi)_{0.9}Ti_{0.1}$, $(CoCrNi)_{0.9}Mo_{0.1}$, and $(CoCrNi)_{0.9}W_{0.1}$ are 36, 48, 28, and 30 GPa, respectively, demonstrating that Ti has a significant effect in reducing C_{11}. Alloying Ti also results in a significant decrease in C_{44} but has little effect on C_{12}.

On the basis of the calculated elastic constants, the elastic properties, including the shear modulus (G), bulk modulus (B), Poisson's ratio, and Young's modulus (E), of the CoCrNi-based alloys with different alloying additions were obtained, and the results are plotted in Fig. 5. The calculated shear modulus of CoCrNi is 104 GPa, which is in good agreement with the calculated value of 105 GPa at 0 K by Ge *et al*. [31] and extrapolated experimental data of 94 GPa by Laplanche *et al*. [42]. Alloying Al, Ti, Mo, and W to the CoCrNi alloy results in a decrease in the shear modulus, as shown in Fig. 5a. It is noted that the decrease of shear modulus by Ti is much larger than that by Al, Mo, and W at the same concentration. The Young's modulus and bulk modulus also decrease with the alloying addition of Al, Ti, Mo, and W, whereas the Poisson's ratio shows an opposite trend.

For the description of solute strengthening of fcc HEAs, Varvenne *et al*. [16] modified a Labusch-type model, which has been applied with good quantitative success to HEAs. Based on this model, the zero-temperature shear stress (τ_{y0}) of HEAs can be described by

$$\tau_{y0} = A_\tau \alpha^{-\frac{1}{3}} G\left(\frac{1+\nu}{1-\nu}\right)^{\frac{4}{3}} f\left[\frac{\delta}{b^6}\right]^{\frac{2}{3}} \tag{14}$$

where b is the Burger's vector (see Table 1), ν is the Poisson's ratio, and A_τ, α, and f are coefficients (their values are 0.051, 0.06125, and 0.35, respectively) [16]. The shear stresses of the CoCrNi alloys with different alloying additions are tabulated in Table 4. The calculated shear stress of $(CoCrNi)_{0.9}W_{0.1}$ is 0.795 GPa, which is comparable to that of $(CoCrNi)_{0.9}Mo_{0.1}$ (0.650 GPa) but much larger than that of $(CoCrNi)_{0.9}Ti_{0.1}$ (0.393 GPa), $(CoCrNi)_{0.9}Al_{0.1}$ (0.258 GPa), and CoCrNi (0.170 GPa), indicating that the W and Mo additions remarkably enhance the shear stress of the CoCrNi-based alloys.

The Taylor factor for fcc polycrystals is approximately 3.06 [16], so the yield stress of the CoCrNi-based alloys (σ_{alloy}) can be estimated by

$$\sigma_{alloy} = 3.06\tau_{y0}\,. \tag{15}$$

The yield stress of the CoCrNi-based alloys is shown in Fig. 6 as a function of the Al, Ti, Mo, and W additions. The calculated yield stress of CoCrNi is 0.519 GPa at 0 K, which is close to the experimental value of 0.560 GPa at 77 K, as obtained by Laplanche *et al*. [25]. The yield stress of the CoCrNi-based alloys increases almost linearly with the Al addition, which is in good agreement with the experimental fitting results [40], indicating that our predictions are reliable. From Fig. 6,

it is evident that the yield stress of the CoCrNi-based alloys increases with increasing contents of Al, Ti, Mo, and W. In addition, the yield stress of the $(CoCrNi)_{100-x}Mo_x$ and $(CoCrNi)_{100-x}W_x$ alloys is larger than that of the $(CoCrNi)_{100-x}Al_x$ and $(CoCrNi)_{100-x}Ti_x$ alloys at the same alloying content, suggesting that Mo and W have a higher strengthening efficiency than Ti and Al in the fcc MEAs.

3.3 SFE and deformation behavior

The compositional dependence of USFE of the CoCrNi-based alloys are displayed in Fig. 7a. The USFE of CoCrNi is 339 mJ/m^2, which is close to the value of 313 mJ/m^2 calculated by Huang *et al* [43]. Alloying Al, Ti, Mo, and W to the CoCrNi alloy results in a decrease in the USFE. In particular, the USFEs of $(CoCrNi)_{0.9}Al_{0.1}$, $(CoCrNi)_{0.9}Ti_{0.1}$, $(CoCrNi)_{0.9}Mo_{0.1}$, and $(CoCrNi)_{0.9}W_{0.1}$ are 287, 247, 287, and 297 mJ/m^2, respectively, indicating that Ti leads to a much larger decrease in USFE than Al, Mo, and W.

The compositional dependences of ISFE of the CoCrNi-based alloys are illustrated in Fig. 7b. The calculated ISFE of CoCrNi is -29 mJ/m^2 at 0 K, which agrees well with the reported data of -26 mJ/m^2 by Huang *et al*. [43] and -24 mJ/m^2 by Yang *et al*. [44]. For fcc structures, ISFs can be regarded as an hcp structure embedded in an fcc matrix. Thus, the strain-induced fcc-to-hcp transformation is likely to form when the ISFE approaches to negative values. With addition of Al, the ISFE increases from -29 mJ/m^2 for the CoCrNi alloy to -19 mJ/m^2 for the $(CoCrNi)_{0.96}Al_{0.04}$ alloy and to -14 mJ/m^2 for the $(CoCrNi)_{0.9}Al_{0.1}$ alloy. This trend is in consistent to that calculated in the CoCrFeNi-Al and CoCrFeNiMn-Al alloys [35, 45], in which the ISFE increases with the Al

content. In contrast, the ISFEs of the CoCrNi-based alloys decrease with increasing Mo content, from -29 mJ/m^2 for the CoCrNi alloy to -38 mJ/m^2 for the $(CoCrNi)_{0.96}Mo_{0.04}$ alloy and to -48 mJ/m^2 for the $(CoCrNi)_{0.9}Mo_{0.1}$ alloy. The large negative ISFEs of the Mo-containing alloys indicate that Mo promotes the formation of stacking faults in the CoCrNi-based alloys. On the contrary, Ti and W have little effect on the ISFEs of the CoCrNi-based alloys.

The energy barrier for dislocation slips, which is defined as the energy difference between USFE and ISFE (γ_{usf} -γ_{isf}), plays an important role in determining the mobility of a slip system. A low slip energy barrier corresponds to a high dislocation mobility of the slip system. In this work, we calculated the effects of the Al, Ti, Mo, and W additions on the slip energy barrier of the CoCrNi-based alloys. The compositional dependences of the slip energy barrier of the CoCrNi-based alloy are also summarized in Table 4. It is evident that alloying Al, Ti, Mo, and W to CoCrNi results in a decrease in the slip energy barrier. In particular, Al and Ti lead to a larger decrease of the slip energy barrier than Mo and W.

The dimensionless parameter (γ_d) proposed by Jo *et al*. [46] has been successfully used to understand the deformation behavior of the CoCrNi-based MEAs [44] and CoCrFeNi-Al HEAs [45] in previous studies. This parameter was used to quantify the effects of the Al, Ti, Mo, and W additions on the deformation behavior of the CoCrNi-based alloys. The γ_d is defined as the ratio of the ISFE (γ_{isf}) to the slip energy barrier (γ_{usf} -γ_{isf}), which can be expressed by

$$\gamma_d = \frac{\gamma_{isf}}{\gamma_{usf} - \gamma_{isf}}. \quad (16)$$

The negative values of γ_d represent that the ISFs are energetically favored to form. A full slip and stacking faults can be combined when the γ_d is between -0.5 and 0, where only stacking faults occur when the γ_d is below -0.5. The γ_d of the CoCrNi-based alloys is illustrated in Fig. 8 as a function of alloying additions. The γ_d of CoCrNi is -0.079. With the Al additions, the γ_d increases to -0.055 for the $(CoCrNi)_{0.96}Al_{0.04}$ alloy and to -0.046 for the $(CoCrNi)_{0.9}Al_{0.1}$ alloy. These results suggest that more dislocations would form in the CoCrNi-based MEAs with Al additions. In contrast, Ti and W have very limited effects on the γ_d when their mole fractions are varied from 0 to 10 at.%. Experimentally, a high density of dislocations with no deformation twins or stacking faults was observed in a $(CoCrNi)_{0.93}Al_{0.04}Ti_{0.02}Nb_{0.01}$ alloy by Slone *et al*. [47], whereas a high density of nanotwins and stacking faults was detected in a CoCrNi alloy by Laplanche *et al*. [25]. Thus, the predicted deformation behavior is consistent with the experimental findings. In addition, it is interesting to note that Mo reduces the γ_d of the CoCrNi-based alloys, indicating that Mo would enhance the formation of stacking faults. Recently, experimental observations confirmed that a higher density of SFs is formed in a $(CoCrNi)_{0.97}Mo_{0.03}$ alloy as compared with a Mo-free alloy during tensile deformation [48], which is in good agreement with our theoretical predictions. Therefore, our calculations suggest that the Al and Mo additions result in a significant change in the formation of stacking faults in the CoCrNi-based alloys, which would have an important impact on the deformation behavior of these alloys. It should be pointed out that the CoCrNi-based alloys are metastable; for these alloys, first-principles calculations predict negative SFE values, which cannot be validated by the existing experimental methods, such as TEM analysis, because the

experimental methods for determining SFE presuppose that SFE is positive [49,50]. The experimental validation of SFEs of metastable materials is still a challenging and unsolved problem. In addition, the influence of local chemical and structural environments on the deformation behavior was ignored in this work, since our calculations are focused on the comparative study of the alloying effects of Al, Ti, Mo, and W. Several investigations indicate that the M/HEAs possess complicated local environments, including chemical ordering and local lattice distortions, which can influence the physical properties of M/HEAs [10,51]. Thus, it is possible that the local environments induced by alloying additions may also play a role in the phase stability, mechanical properties, and deformation behavior of M/HEAs, which, however, is out of the scope of the present work; we will systematically investigate these issues in our future study.

4. Conclusions

The effects of the Al, Ti, Mo, and W additions on the phase stability, mechanical properties, and deformation behavior of CoCrNi-based MEAs at low temperatures were systematically studied by using the density functional theory implemented within the EMTO-CPA method. The compositional dependence of phase stability was explored by comparing the total energies of the bcc, fcc, and hcp phases. The solute strengthening of alloying additions was evaluated in terms of the lattice distortion and elastic property mismatch. Furthermore, the effects of alloying additions on the SFEs of the CoCrNi-based alloys were calculated. The following conclusions can be drawn from this study.

1. The formation of hcp phase is more energetically favorable than the fcc phase in the $CoCrNiM_x$ (M = Al, Ti, Mo, and W; $x = 0 – 0.1$) alloys at 0 K. Mo acts as an hcp stabilizer in the CoCrNi-based MEAs, whereas Al, Ti, and W improve the phase stability of the fcc phase.
2. The Al, Ti, Mo, and W additions influence the lattice distortion and elastic properties of the MEAs, thereby affecting the solute strengthening effect. The lattice distortion of the CoCrNi-based alloys is sensitive to the effective volume of the alloying elements. In particular, the effective volumes of W and Mo is larger than those of Al and Ti, leading to a large lattice distortion in the CoCrNi-based alloys. In addition, the reduction of elastic properties by Ti is much larger than that by Al, Mo, and W. Based on the Labusch-type model, we show that the strengthening effect of alloying elements decreases in the order W > Mo > Ti > Al, suggesting that the lattice distortion factor dominates the strengthening effect of Al, Ti, Mo, and W in the CoCrNi-based MEAs.
3. Alloying Al, Ti, Mo, and W to the CoCrNi alloy results in a decrease in the USFE. The ISFE increases with the Al, Ti, and W additions but decreases with the Mo additions. The variations of ISFE are lower than those of USFE, leading to a reduction of the slip energy barrier. By using the dimensionless parameter defined as the ratio of the ISFE to slip energy barrier, our calculations reveal that Mo enhances the formation of stacking faults, whereas Al favors the occurrence of both dislocation slip and stacking faults.

Acknowledgements

This research was supported by the National Natural Science Foundation of China (no. 52171162), Research Grants Council of Hong Kong (ECS project no. 25202719 and GRF projects no. 15227121 and no. 152190/18E), State Key Laboratory for Advanced Metals and Materials Open Fund (2021-ZD04), State Key Laboratory of Long-life High Temperature Materials (P0036623), and PolyU internal funds (P0009738, P0000538, and P0013994).

References

[1] J.W. Yeh, S.K. Chen, S.J. Lin, J.Y. Gan, T.S. Chin, T.T. Shun, C.H. Tsau, S.Y. Chang, Nanostructured High-Entropy Alloys with Multiple Principal Elements: Novel Alloy Design Concepts and Outcomes, Adv. Eng. Mater. 6(5) (2004) 299-303.

[2] Y. Zhang, T.T. Zuo, Z. Tang, M.C. Gao, K.A. Dahmen, P.K. Liaw, Z.P. Lu, Microstructures and properties of high-entropy alloys, Prog. Mater. Sci. 61 (2014) 1-93.

[3] E.P. George, D. Raabe, R.O. Ritchie, High-entropy alloys, Nat. Rev. Mater. 4(8) (2019) 515-534.

[4] Z.P. Lu, H. Wang, M.W. Chen, I. Baker, J.W. Yeh, C.T. Liu, T.G. Nieh, An assessment on the future development of high-entropy alloys: Summary from a recent workshop, Intermetallics 66 (2015) 67-76.

[5] Q. Lin, J. Liu, X. An, H. Wang, Y. Zhang, X. Liao, Cryogenic-deformation-induced phase transformation in an FeCoCrNi high-entropy alloy, Mater. Res. Lett. 6(4) (2018) 236-243.

[6] B. Gludovatz, A. Hohenwarter, D. Catoor, E.H. Chang, E.P. George, R.O. Ritchie, A fracture-resistant high-entropy alloy for cryogenic applications, Science 345(6201) (2014) 1153.

[7] A. Gali, E.P. George, Tensile properties of high- and medium-entropy alloys, Intermetallics 39 (2013) 74-78.

[8] B. Gludovatz, A. Hohenwarter, K.V.S. Thurston, H. Bei, Z. Wu, E.P. George, R.O. Ritchie, Exceptional damage-tolerance of a medium-entropy alloy CrCoNi at cryogenic temperatures, Nat. Commun. 7(1) (2016) 10602.

[9] D. Wei, X. Li, J. Jiang, W. Heng, Y. Koizumi, W.-M. Choi, B.-J. Lee, H.S. Kim, H. Kato, A. Chiba, Novel Co-rich high performance twinning-induced plasticity (TWIP) and transformation-induced plasticity (TRIP) high-entropy alloys, Scr. Mater. 165 (2019) 39-43.

[10] Z. Lei, X. Liu, Y. Wu, H. Wang, S. Jiang, S. Wang, X. Hui, Y. Wu, B. Gault, P. Kontis, D. Raabe, L. Gu, Q. Zhang, H. Chen, H. Wang, J. Liu, K. An, Q. Zeng, T.-G. Nieh, Z. Lu, Enhanced strength and ductility in a high-entropy alloy via ordered oxygen complexes, Nature 563(7732) (2018) 546-550.

[11] Z. Li, K.G. Pradeep, Y. Deng, D. Raabe, C.C. Tasan, Metastable high-entropy dual-phase alloys overcome the strength-ductility trade-off, Nature 534(7606) (2016) 227-230.

[12] T. Yang, Y.L. Zhao, Y. Tong, Z.B. Jiao, J. Wei, J.X. Cai, X.D. Han, D. Chen, A. Hu, J.J. Kai, K. Lu, Y. Liu, C.T. Liu, Multicomponent intermetallic nanoparticles and superb mechanical behaviors of complex alloys, Science 362(6417) (2018) 933.

[13] L. Fan, T. Yang, Y. Zhao, J. Luan, G. Zhou, H. Wang, Z. Jiao, C.-T. Liu, Ultrahigh strength and ductility in newly developed materials with coherent nanolamellar architectures, Nat. Commun. 11(1) (2020) 6240.

[14] Y. Ma, Q. Wang, X. Zhou, J. Hao, B. Gault, Q. Zhang, C. Dong, T.G. Nieh, A Novel Soft-Magnetic B2-Based Multiprincipal-Element Alloy with a Uniform Distribution of Coherent Body-Centered-Cubic Nanoprecipitates, Adv. Mater. 33(14) (2021) 2006723.

[15] I. Toda-Caraballo, P.E.J. Rivera-Díaz-del-Castillo, Modelling solid solution hardening in high entropy alloys, Acta Mater. 85 (2015) 14-23.

[16] C. Varvenne, A. Luque, W.A. Curtin, Theory of strengthening in fcc high entropy alloys, Acta Mater. 118 (2016) 164-176.

[17] Z. Wu, H. Bei, G.M. Pharr, E.P. George, Temperature dependence of the mechanical properties of equiatomic solid solution alloys with face-centered cubic crystal structures, Acta Mater. 81 (2014) 428-441.

[18] F. Otto, A. Dlouhý, C. Somsen, H. Bei, G. Eggeler, E.P. George, The influences of temperature and microstructure on the tensile properties of a CoCrFeMnNi high-entropy alloy, Acta Mater. 61(15) (2013) 5743-5755.

[19] Z. Yang, J. Sun, S. Lu, L. Vitos, A comparative study of solid-solution strengthening in Cr-Co-Ni complex concentrated alloys: The effect of magnetism, Comput. Mater. Sci. 192 (2021) 110408.

[20] D. Wei, X. Li, S. Schönecker, J. Jiang, W.-M. Choi, B.-J. Lee, H.S. Kim, A. Chiba, H. Kato, Development of strong and ductile metastable face-centered cubic single-phase high-entropy alloys, Acta Mater. 181 (2019) 318-330.

[21] S. Huang, H. Huang, W. Li, D. Kim, S. Lu, X. Li, E. Holmström, S.K. Kwon, L. Vitos, Twinning in metastable high-entropy alloys, Nat. Commun. 9(1) (2018) 2381.

[22] S. Kibey, J.B. Liu, D.D. Johnson, H. Sehitoglu, Predicting twinning stress in fcc metals: Linking twin-energy pathways to twin nucleation, Acta Mater. 55(20) (2007) 6843-6851.

[23] H. He, M. Naeem, F. Zhang, Y. Zhao, S. Harjo, T. Kawasaki, B. Wang, X. Wu, S. Lan, Z. Wu, W. Yin, Y. Wu, Z. Lu, J.-J. Kai, C.-T. Liu, X.-L. Wang, Stacking Fault Driven Phase Transformation in CrCoNi Medium Entropy Alloy, Nano Lett. 21(3) (2021) 1419-1426.

[24] Y.H. Zhang, Y. Zhuang, A. Hu, J.J. Kai, C.T. Liu, The origin of negative stacking fault energies and nano-twin formation in face-centered cubic high entropy alloys, Scr. Mater. 130 (2017) 96-99.

[25] G. Laplanche, A. Kostka, C. Reinhart, J. Hunfeld, G. Eggeler, E.P. George, Reasons for the superior mechanical properties of medium-entropy CrCoNi compared to high-entropy CrMnFeCoNi, Acta Mater. 128 (2017) 292-303.

[26] Y.J. Zhou, Y. Zhang, Y.L. Wang, G.L. Chen, Solid solution alloys of AlCoCrFeNiTix with excellent room-temperature mechanical properties, Appl. Phys. Lett. 90(18) (2007) 181904.

[27] C. Li, J.C. Li, M. Zhao, Q. Jiang, Effect of aluminum contents on microstructure and properties of AlxCoCrFeNi alloys, J. Alloys Compd. 504 (2010) S515-S518.

[28] Z. Wu, W. Guo, K. Jin, J.D. Poplawsky, Y. Gao, H. Bei, Enhanced strength and ductility of a tungsten-doped CoCrNi medium-entropy alloy, J. Mater. Res. 33(19) (2018) 3301-3309.

[29] X. Li, Z. Li, Z. Wu, S. Zhao, W. Zhang, H. Bei, Y. Gao, Strengthening in Al-, Mo- or Ti-doped CoCrFeNi high entropy alloys: A parallel comparison, J. Mater. Sci. Technol. 94 (2021) 264-274.

[30] L. Vitos, Total-energy method based on the exact muffin-tin orbitals theory, Phys. Rev. B 64(1) (2001) 014107.

[31] H. Ge, H. Song, J. Shen, F. Tian, Effect of alloying on the thermal-elastic properties of 3d high-entropy alloys, Mater. Chem. Phys. 210 (2018) 320-326.

[32] S. Qiu, S.-M. Chen, M. Naihua, J. Zhou, Q.-M. Hu, Z. Sun, Structural stability and mechanical properties of B2 ordered refractory AlNbTiVZr high entropy alloys, J. Alloys Compd. (2021) 161289.

[33] B.L. Gyorffy, A.J. Pindor, J. Staunton, G.M. Stocks, H. Winter, A first-principles theory of ferromagnetic phase transitions in metals, J. phys., F Met. phys. 15(6) (1985) 1337-1386.

[34] J.P. Perdew, K. Burke, M. Ernzerhof, Generalized Gradient Approximation Made Simple, Phys. Rev. Lett. 77(18) (1996) 3865-3868.

[35] S. Qiu, X.-C. Zhang, J. Zhou, S. Cao, H. Yu, Q.-M. Hu, Z. Sun, Influence of lattice distortion on stacking fault energies of CoCrFeNi and Al-CoCrFeNi high entropy alloys, J. Alloys Compd. 846 (2020) 156321.

[36] S. Huang, E. Holmström, O. Eriksson, L. Vitos, Mapping the magnetic transition temperatures for medium- and high-entropy alloys, Intermetallics 95 (2018) 80-84.

[37] S.F. Liu, Y. Wu, H.T. Wang, J.Y. He, J.B. Liu, C.X. Chen, X.J. Liu, H. Wang, Z.P. Lu, Stacking fault energy of face-centered-cubic high entropy alloys, Intermetallics 93 (2018) 269-273.

[38] F. Zhang, Y. Wu, H. Lou, Z. Zeng, V.B. Prakapenka, E. Greenberg, Y. Ren, J. Yan, J.S. Okasinski, X. Liu, Y. Liu, Q. Zeng, Z. Lu, Polymorphism in a high-entropy alloy, Nat. Commun. 8(1) (2017) 15687.

[39] D. Ma, B. Grabowski, F. Körmann, J. Neugebauer, D. Raabe, Ab initio thermodynamics of the CoCrFeMnNi high entropy alloy: Importance of entropy contributions beyond the configurational one, Acta Mater. 100 (2015) 90-97.

[40] M.P. Agustianingrum, S. Yoshida, N. Tsuji, N. Park, Effect of aluminum addition on solid solution strengthening in CoCrNi medium-entropy alloy, J. Alloys Compd. 781 (2019) 866-872.

[41] C. Varvenne, W.A. Curtin, Strengthening of high entropy alloys by dilute solute additions: CoCrFeNiAlx and CoCrFeNiMnAlx alloys, Scr. Mater. 138 (2017) 92-95.

[42] G. Laplanche, P. Gadaud, C. Bärsch, K. Demtröder, C. Reinhart, J. Schreuer, E.P. George, Elastic moduli and thermal expansion coefficients of medium-entropy subsystems of the CrMnFeCoNi high-entropy alloy, J. Alloys Compd. 746 (2018) 244-255.

[43] H. Huang, X. Li, Z. Dong, W. Li, S. Huang, D. Meng, X. Lai, T. Liu, S. Zhu, L. Vitos, Critical stress for twinning nucleation in CrCoNi-based medium and high entropy alloys, Acta Mater. 149 (2018) 388-396.

[44] Z. Yang, S. Lu, Y. Tian, Z. Gu, H. Mao, J. Sun, L. Vitos, Assessing the magnetic order dependent γ-surface of Cr-Co-Ni alloys, J. Mater. Sci. Technol. 80 (2021) 66-74.

[45] X. Sun, H. Zhang, W. Li, X. Ding, Y. Wang, L. Vitos, Generalized Stacking Fault Energy of Al-Doped CrMnFeCoNi High-Entropy Alloy, Nanomaterials 10(1) (2020).

[46] M. Jo, Y.M. Koo, B.-J. Lee, B. Johansson, L. Vitos, S.K. Kwon, Theory for plasticity of face-centered cubic metals, Proc. Natl. Acad. Sci. U.S.A. 111(18) (2014) 6560.

[47] C.E. Slone, C.R. LaRosa, C.H. Zenk, E.P. George, M. Ghazisaeidi, M.J. Mills, Deactivating deformation twinning in medium-entropy CrCoNi with small additions of aluminum and titanium, Scr. Mater. 178 (2020) 295-300.

[48] R. Chang, W. Fang, J. Yan, H. Yu, X. Bai, J. Li, S. Wang, S. Zheng, F. Yin, Microstructure and mechanical properties of CoCrNi-Mo medium entropy alloys: Experiments and first-principle calculations, J. Mater. Sci. Technol. 62 (2021) 25-33.

[49] K.V. Werner, F. Niessen, M. Villa, M.A. Somers, Experimental validation of negative stacking fault energies in metastable face-centered cubic materials, Appl. Phys. Lett. 119 (2021) 141902.

[50] X. Sun, S. Lu, R. Xie, X. An, W. Li, T. Zhang, C. Liang, X. Ding, Y. Wang, H. Zhang, L. Vitos, Can experiment determine the stacking fault energy of metastable alloys? Mater. Des. 199 (2021) 109396.

[51] S.D. Wang, X.J. Liu, Z.F. Lei, D.Y. Lin, F.G. Bian, C.M. Yang, M.Y. Jiao, Q. Du, H. Wang, Y. Wu, S.H. Jiang, Z.P. Lu, Chemical short-range ordering and its strengthening effect in refractory high-entropy alloys, Phys. Rev. B 103(10) (2021) 104107.

Figure Captions

Fig. 1. Schematic of planar fault path on (111) planes for the calculation of SFEs of the 6-layer fcc structure, with (a) for the ideal fcc structure, (b) for the defective structure with a USF, and (c) for the defective structure with an ISF.

Fig. 2. Theoretical Wigner-Seitz (W-S) radii of the CoCrNi-based alloys as a function of the Al, Ti, Mo, and W contents.

Fig. 3. Theoretical energy differences (a) between the hcp and fcc phases (E_{hcp} - E_{fcc}) and (b) between the bcc and fcc phases (E_{bcc} - E_{fcc}) of the CoCrNi-based alloys as a function of the Al, Ti, Mo and W contents.

Fig. 4. The schematic for random occupancy of atoms with different atomic volumes and lattice of atoms with an equivalent average atomic volume.

Fig. 5. Elastic properties of the CoCrNi-based alloys as a function of alloying additions: (a) shear modulus (G), (b) bulk modulus (B), (c) Poisson's ratio, and (d) Young's modulus (E).

Fig. 6. Calculated yield stresses of the CoCrNi-based alloys as a function of the Al, Ti, Mo and W contents.

Fig. 7. (a) USFEs and (b) ISFEs of the CoCrNi-based alloys with different Al, Ti, Mo, and W contents at 0 K.

Fig. 8. The γ_d of the CoCrNi-based alloys as a function of the Al, Ti, Mo and W contents.

Fig. 1

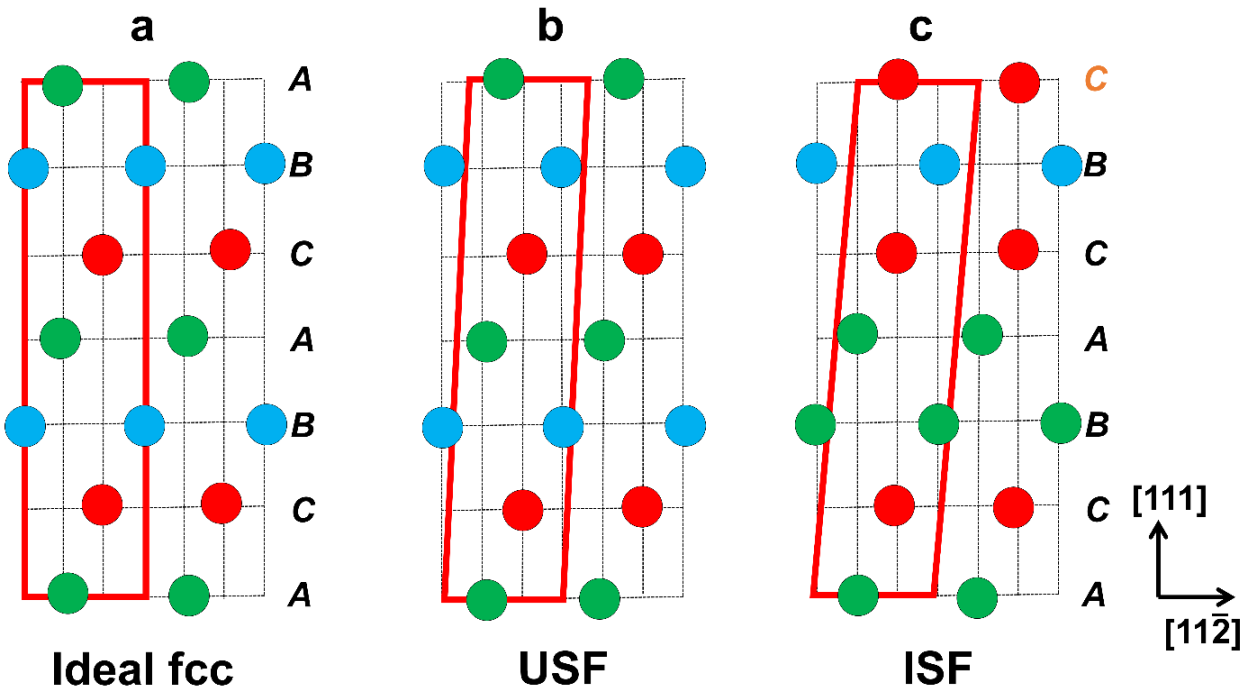

Fig. 2

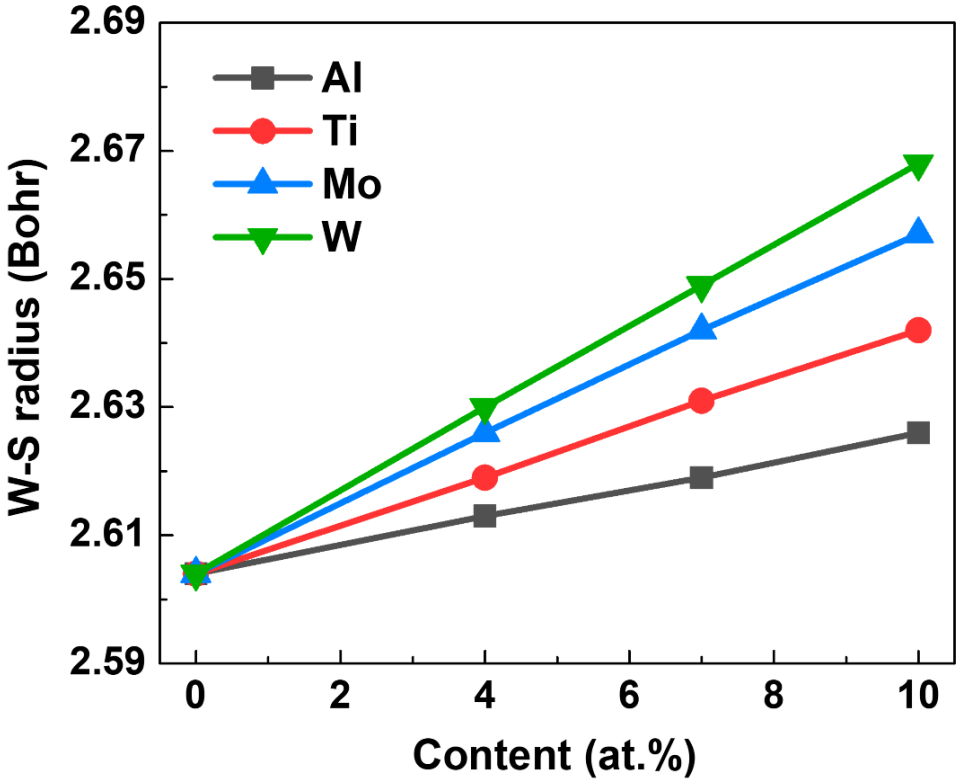
2.69
2.67
2.65
2.63
2.61
2.59
W-S radius (Bohr)
Al
Ti
Mo
W
0
2
4
6
8
10
Content (at.%)

Fig. 3

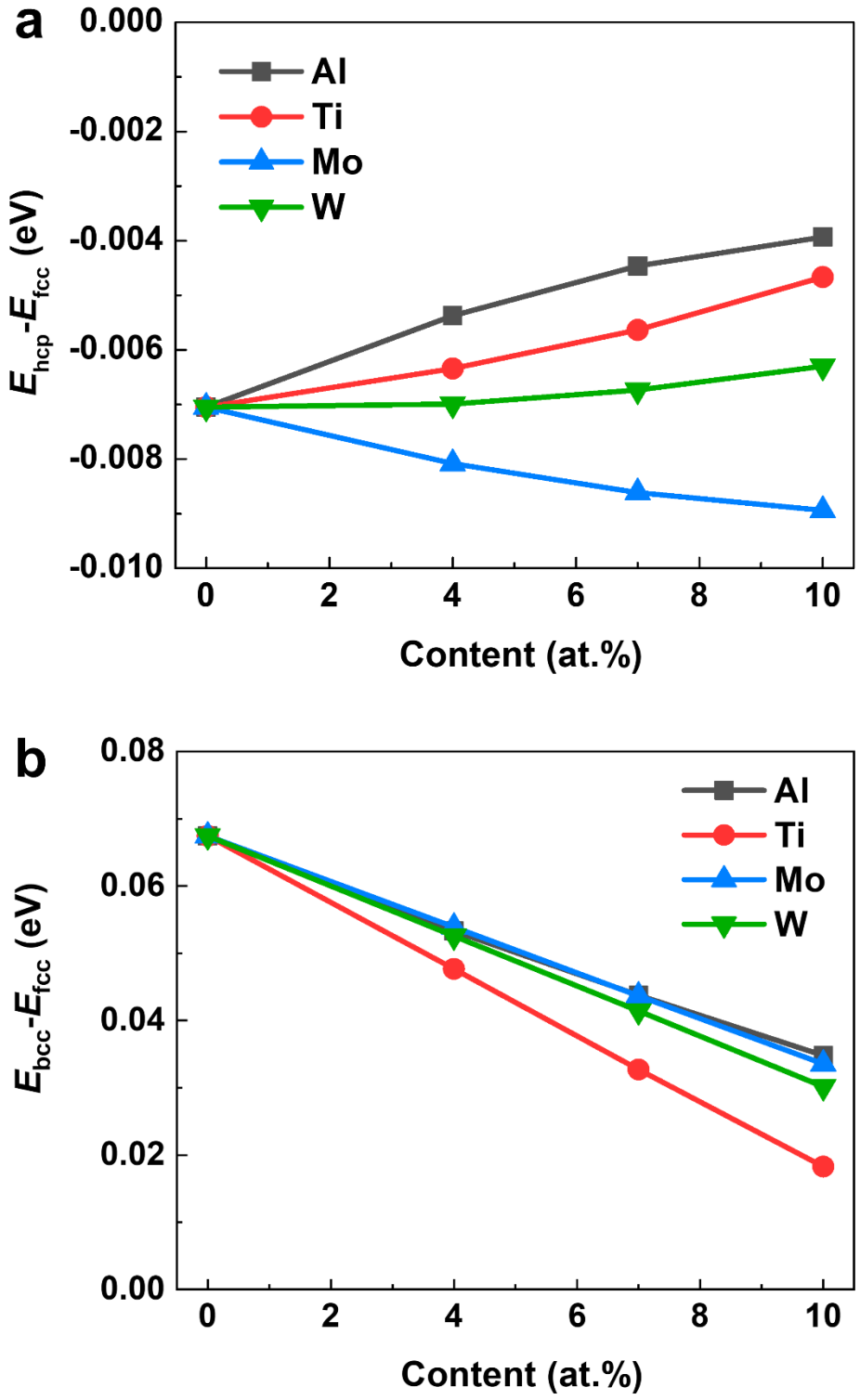
a
0.000
-0.002
-0.004
-0.006
-0.008
-0.010
E_{hcp}-E_{fcc} (eV)
Al
Ti
Mo
W
0
2
4
6
8
10
Content (at.%)
b
0.08
0.06
0.04
0.02
0.00
E_{bcc}-E_{fcc} (eV)
Al
Ti
Mo
W
0
2
4
6
8
10
Content (at.%)

Fig. 4

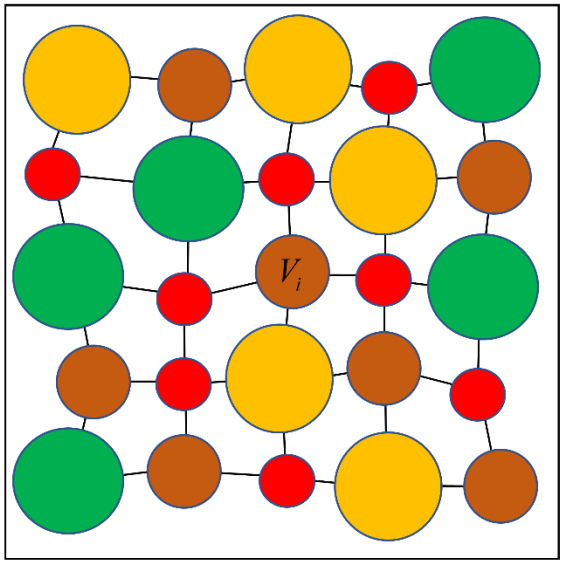

Random occupancy of atoms with different atomic volumes

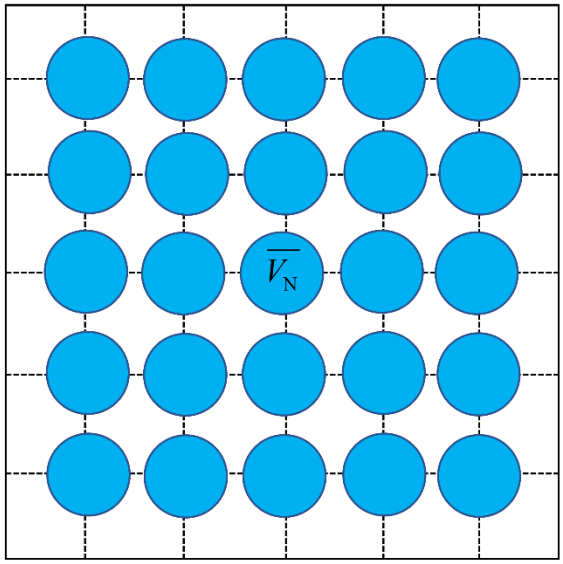

Lattice of atoms with equivalent average atomic volume

Fig. 5

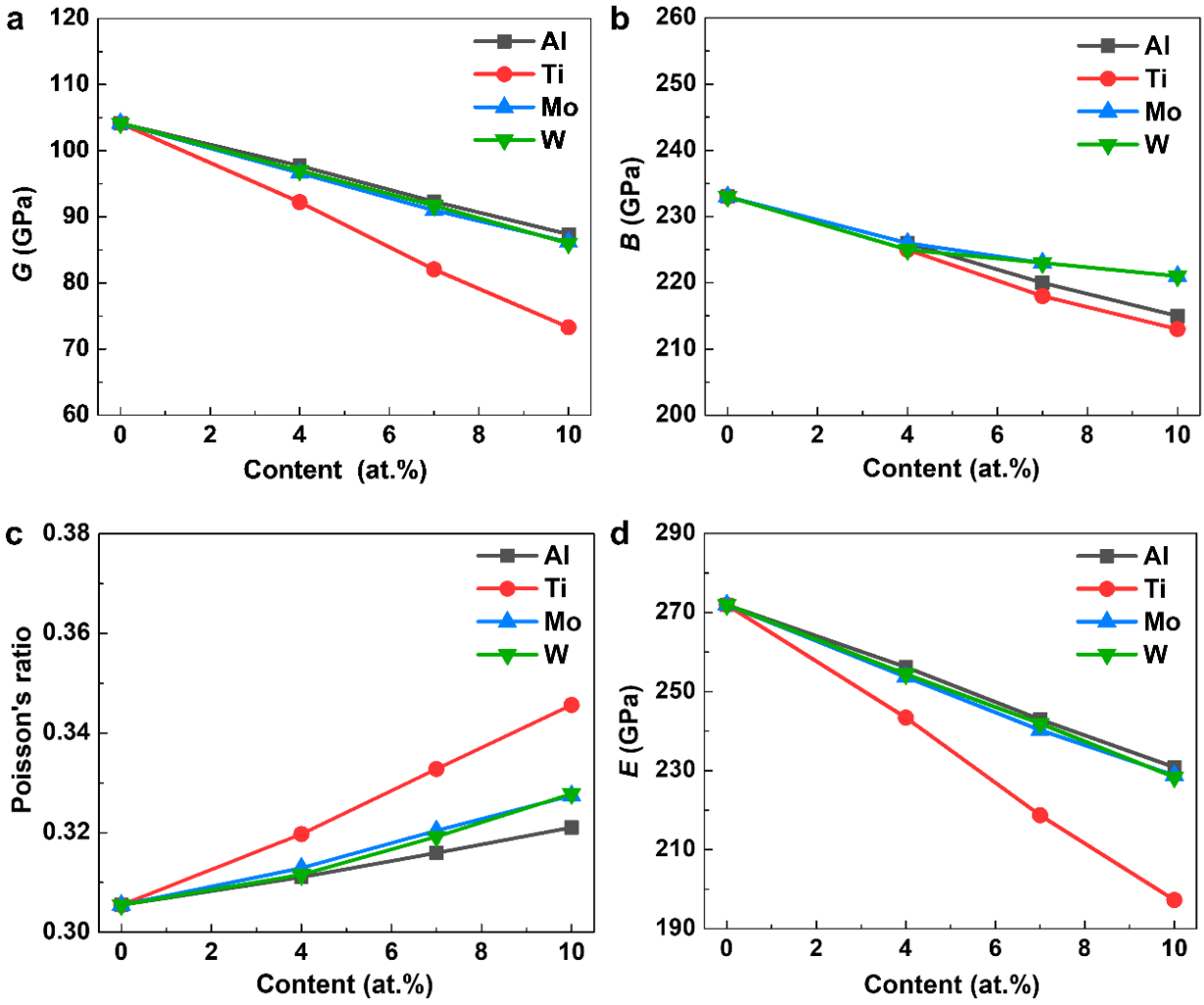
a
G (GPa)
Content (at.%)
Al
Ti
Mo
W
b
B (GPa)
Content (at.%)
c
Poisson's ratio
Content (at.%)
d
E (GPa)
Content (at.%)

Fig. 6

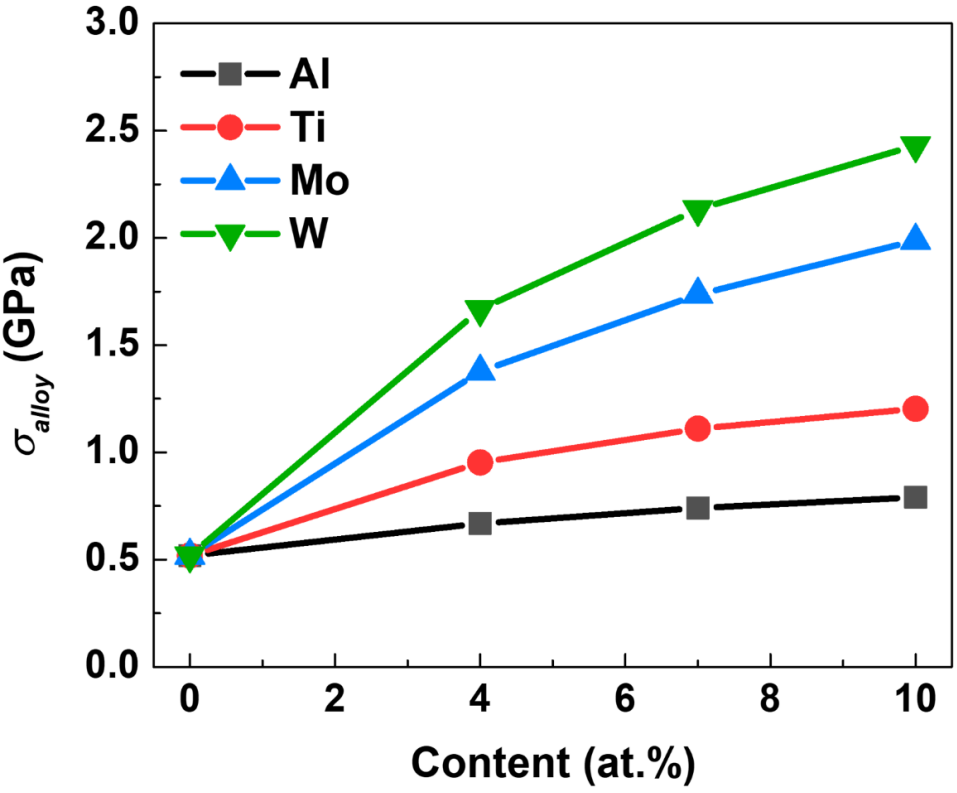
3.0
2.5
2.0
1.5
1.0
0.5
0.0
σ_{alloy} (GPa)
Al
Ti
Mo
W
0
2
4
6
8
10
Content (at.%)

Fig. 7

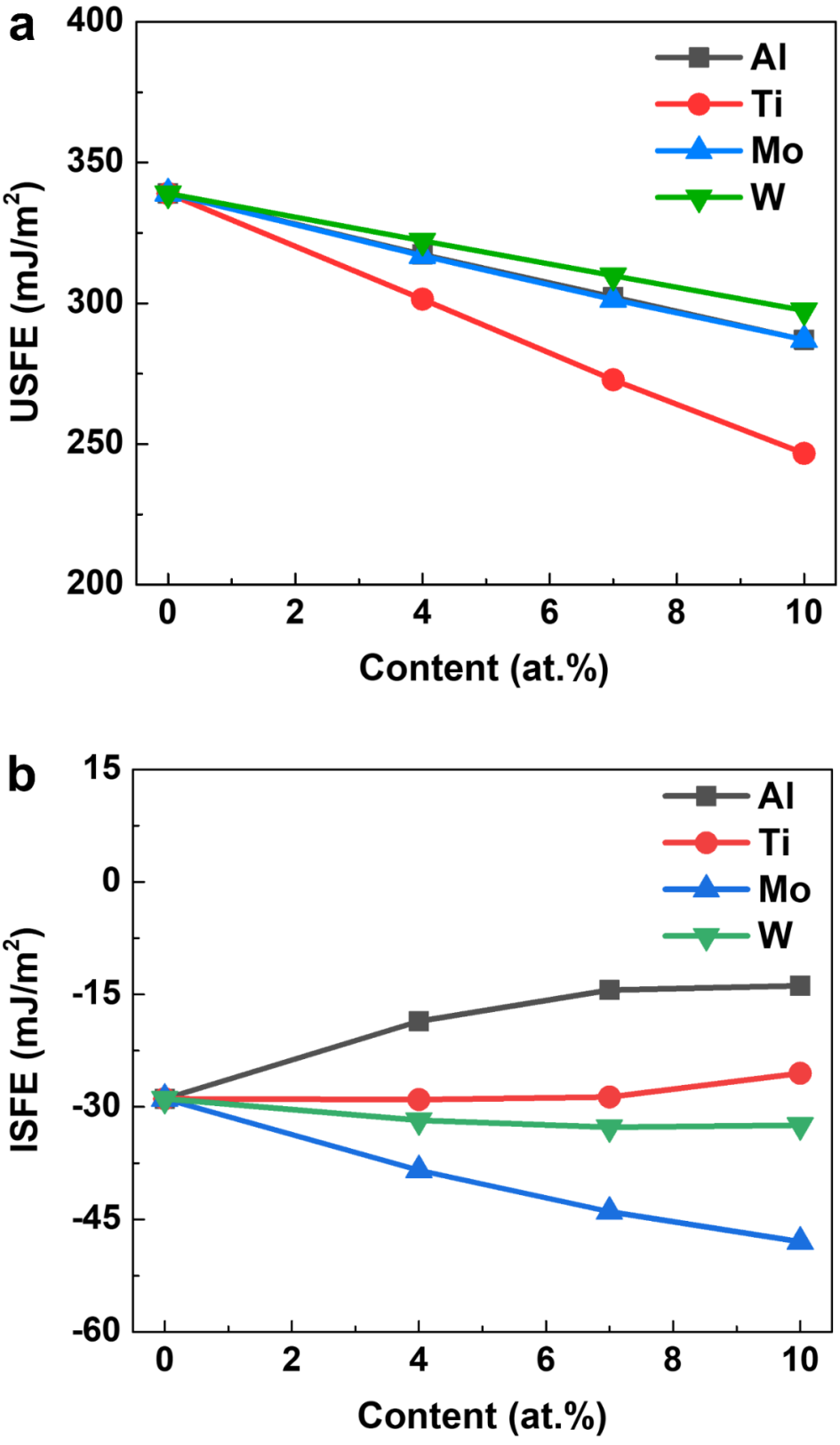
a
400
350
300
250
200
USFE (mJ/m^2)
0
2
4
6
8
10
Content (at.%)
Al
Ti
Mo
W
b
15
0
-15
-30
-45
-60
ISFE (mJ/m^2)
0
2
4
6
8
10
Content (at.%)
Al
Ti
Mo
W

Fig. 8

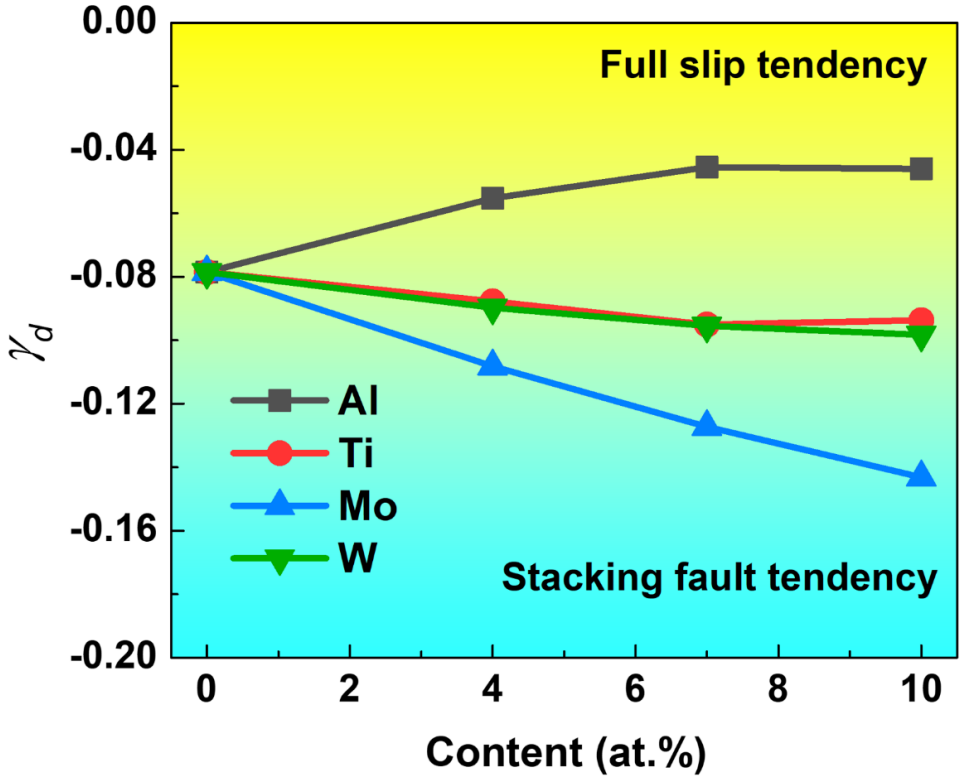
0.00
-0.04
-0.08
-0.12
-0.16
-0.20
γ_d
Full slip tendency
Stacking fault tendency
Al
Ti
Mo
W
0
2
4
6
8
10
Content (at.%)

Table 1. W-S radii, Burger's vectors (b), alloy volumes ($\overline{V_N}$), and lattice distortions (δ) of the CoCrNi-based alloys with different Al, Ti, Mo, and W additions.

Composition	W-S radius (Bohr)	b (Bohr)	$\overline{V_N}$ (Bohr^3/atom)	δ
CoCrNi	2.604	4.712	74.0	21.1
$(CoCrNi)_{0.96}Al_{0.04}$	2.613	4.728	74.7	33.8
$(CoCrNi)_{0.93}Al_{0.07}$	2.619	4.739	75.2	42.6
$(CoCrNi)_{0.9}Al_{0.1}$	2.626	4.751	75.9	50.7
$(CoCrNi)_{0.96}Ti_{0.04}$	2.619	4.739	75.2	61.3
$(CoCrNi)_{0.93}Ti_{0.07}$	2.631	4.760	76.3	89.1
$(CoCrNi)_{0.9}Ti_{0.1}$	2.642	4.781	77.2	115.0
$(CoCrNi)_{0.96}Mo_{0.04}$	2.626	4.751	75.9	104.0
$(CoCrNi)_{0.93}Mo_{0.07}$	2.642	4.780	77.2	161.6
$(CoCrNi)_{0.9}Mo_{0.1}$	2.657	4.808	78.6	215.2
$(CoCrNi)_{0.96}W_{0.04}$	2.630	4.759	76.2	139.8
$(CoCrNi)_{0.93}W_{0.07}$	2.649	4.793	77.9	222.2
$(CoCrNi)_{0.9}W_{0.1}$	2.668	4.829	79.5	299.1

Table 2. Effective volumes (*Vn*) of Co, Cr, Ni, Al, Ti, Mo, and W in the CoCrNi-based alloys in unit of $Bohr^3$/atom.

	Co	Cr	Ni	Al	Ti	Mo	W
Vn	69.0	80.1	73.0	92.8	106.7	120.7	129.8

Table 3. Elastic constants of the CoCrNi-based alloys with different Al, Ti, Mo, and W additions.

Composition	C_{11} (GPa)	C_{12} (GPa)	C_{44} (GPa)
CoCrNi	296	202	176
$(CoCrNi)_{0.96}Al_{0.04}$	282	198	170
$(CoCrNi)_{0.93}Al_{0.07}$	270	195	166
$(CoCrNi)_{0.9}Al_{0.1}$	260	192	161
$(CoCrNi)_{0.96}Ti_{0.04}$	277	199	162
$(CoCrNi)_{0.93}Ti_{0.07}$	261	197	151
$(CoCrNi)_{0.9}Ti_{0.1}$	248	196	142
$(CoCrNi)_{0.96}Mo_{0.04}$	282	198	167
$(CoCrNi)_{0.93}Mo_{0.07}$	274	198	161
$(CoCrNi)_{0.9}Mo_{0.1}$	268	198	155
$(CoCrNi)_{0.96}W_{0.04}$	281	197	168
$(CoCrNi)_{0.93}W_{0.07}$	274	198	163
$(CoCrNi)_{0.9}W_{0.1}$	266	198	157

Table 4. Predicted shear stresses and slip energy barriers of the CoCrNi-based alloys with different Al, Ti, Mo, and W additions at 0 K.

Composition	τ_{y0} (GPa)	γ_{usf} -γ_{isf} (mJ/m^2)
CoCrNi	0.170	367.93
$(CoCrNi)_{0.96}Al_{0.04}$	0.218	335.97
$(CoCrNi)_{0.93}Al_{0.07}$	0.242	316.67
$(CoCrNi)_{0.9}Al_{0.1}$	0.258	300.89
$(CoCrNi)_{0.96}Ti_{0.04}$	0.311	330.47
$(CoCrNi)_{0.93}Ti_{0.07}$	0.363	301.50
$(CoCrNi)_{0.9}Ti_{0.1}$	0.393	272.21
$(CoCrNi)_{0.96}Mo_{0.04}$	0.450	355.34
$(CoCrNi)_{0.93}Mo_{0.07}$	0.567	345.31
$(CoCrNi)_{0.9}Mo_{0.1}$	0.650	335.08
$(CoCrNi)_{0.96}W_{0.04}$	0.545	354.02
$(CoCrNi)_{0.93}W_{0.07}$	0.697	342.55
$(CoCrNi)_{0.9}W_{0.1}$	0.795	329.86